Discover Water

RESEARCH Open Access

Sustainable synthesis of CQD-modified ZIF-8 from sago *hampas* for improved methylene blue dye removal

Dayang Norafizan Awang Chee[1,2*], Nur Afiqah Kamaludin[1], Nur Anisa Aida Supian[1], Maya Asyikin Mohamad Arif[1] and Mohamed Afizal Mohamed Amin[2,3]

*Correspondence:
Dayang Norafizan Awang Chee
dnorafizan@unimas.my
[1]Faculty Resource Science and Technology, Universiti Malaysia Sarawak, 94300 Kota Samarahan, Sarawak, Malaysia
[2]Faculty of Engineering, UNIMAS Water Centre (UCW), Universiti Malaysia Sarawak, 94300 Kota Samarahan, Sarawak, Malaysia
[3]Department of Chemical Engineering and Energy Sustainability, Faculty of Engineering, Universiti Malaysia Sarawak, 94300 Kota Samarahan, Sarawak, Malaysia

Abstract

High levels of synthetic dyes like methylene blue (MB) in aquatic ecosystems threaten both environmental stability and human health. This research investigates MB adsorption using a composite material known as Carbon Quantum Dots/Zeolitic Imidazole Framework-8 (CQDs/ZIF-8). The composite was made via hydrothermal synthesis from sago waste and then modified with impregnation. To understand its properties, the composite was analyzed using Scanning Electron Microscopy (SEM), Fourier Transform Infrared Spectroscopy (FTIR), and Ultraviolet-Visible Spectroscopy (UV-Vis). The composite adsorbed MB was observed by changing factors such as initial dye concentration, amount of adsorbent, solution pH, and contact time. Various models were used to analyze the data including linear and non-linear isotherm models (Langmuir, Freundlich, Temkin, Dubinin-Radushkevich) and kinetic models (Pseudo-First-Order, Pseudo-Second-Order, Elovich). Model accuracy was analyzed using the coefficient of determination and error analysis. The best removal rates were 88.60% at pH 10, 91.56% at 5 ppm MB concentration, 93.20% after 80 min, and 82.64% with 30 mg of adsorbent. The non-linear Freundlich isotherm and pseudo-second-order kinetic model fit the data best, with a very high correlation (R^2 = 0.9993). Non-linear models are better suited for predicting how adsorption works compared to linear ones.

Keywords Adsorption, CQDs/ZIF-8, Linear regression, Methylene blue, Non-linear regression, Sago *hampas*

1 Introduction

Water pollution remains a pressing global challenge, harming ecosystems, endangering human health, and limiting access to clean water. Synthetic dyes are a major culprit in degrading water quality worldwide. Over 100,000 dye varieties exist, prized for their ability to impart lasting color and resist fading from sunlight, water, chemicals, and microbes. This makes them indispensable in industries like textiles, food processing, rubber, plastics, cosmetics, and pharmaceuticals. Methylene Blue (MB), a common cationic dye used in silk, wool, and cotton dyeing, poses particular risks: industrial effluents

with high MB levels can devastate water sources if untreated. Colored wastewater blocks light penetration, stifling photosynthesis in aquatic plants. Furthermore, MB is toxic, carcinogenic, and mutagenic, causing respiratory issues, nausea, vomiting, diarrhea, and skin irritation upon exposure [1]. Thus, developing efficient, eco-friendly methods to remove MB from wastewater is critical.

Several treatments have been tested for MB removal, including photocatalysis, coagulation, reverse osmosis, membrane filtration, and adsorption. Adsorption stands out as the most effective because of cost-efficiency, easy to operate, and environmentally benign [2]. The process binds dye molecules to adsorbent surfaces, with efficiency depending on factors like initial dye concentration, pH, adsorbent dose, and contact time. Prior research shows peak MB removal occurs at pH 10, 50 ppm initial concentration, 0.5–70 mg adsorbent doses, and 60–90 min contact times [3, 4].

Metal-Organic Frameworks (MOFs) have emerged as advanced adsorbents due to their high porosity, tunable structures, and large surface areas. ZIF-8, a MOF wit a sodalite topology formed by linking 2-methylimidazole (Hmim) ligands to zinc ions (Zn^{2+}) is particularly promising. It boasts exceptional chemical and thermal stability, in addition of a high surface area and pore volume that boost dye adsorption [5, 6]. Studies report varying MB capacities where Santoso et al. (2021) found 24.57 mg g^{-1} for citric acid-derived ZIF-8 was hard to recover from water and tends to clump, reducing its interfacial area and performance [7–9].

To solve these issues, researchers modify ZIF-8 with carbon-based materials. Composites merge carbon's high surface area, conductivity, and porosity with MOFs' structural benefits, improving adsorption and reusability [10]. Among carbon materials, Carbon Quantum Dots (CQDs) chosen as they are very tiny (< 10 nm), spherical carbon nanoparticles feature strong photoluminescence and abundant surface groups (-OH, -COOH, $-NH_2$) that attract dyes, heavy metals, and organics [11]. CQDs are non-toxic, eco-friendly, and can be sourced from renewable biomass like sago waste [12], banana peels [13], lemon juice [14], broccoli [15], and rice husks [16]. CQDs are synthesized via top-down (e.g., laser ablation) or bottom-up (e.g., hydrothermal) methods. Top-down approaches break down larger carbon structures but require expensive equipment. Bottom-up methods like hydrothermal, microwave-assisted, or ultrasonic-assisted synthesis are simpler, cheaper, and more sustainable [17]. Here, sago waste was chosen as the biomass precursor for its high carbon content [18], and hydrothermal synthesis was used for its simplicity, low cost, and environmental compatibility. The study's goals were to synthesize and characterize ZIF-8, CQDs, and their CQDs/ZIF-8 composite, assess their MB adsorption performance, and clarify the adsorption mechanisms driving MB removal.

2 Materials and methods

2.1 Pretreatment of sago waste

The sago waste used in this study was sourced from Mukah, Sarawak, and underwent a pretreatment process before being utilized. First, the raw material was carefully washed to remove any debris and then dried in an oven at 60 °C for a period of two days. Once dried, the sample was mechanically crushed and ground down into small granules measuring between 2 and 3 mm in size.

2.2 Synthesis of CQDs

Carbon quantum dots (CQDs) were produced using a hydrothermal method, adapting a procedure documented in existing literature [19]. The sago *hampas* was initially rinsed to remove dust and other impurities, then dried in an oven at 60 °C for 48 h and subsequently milled into a fine powder. Approximately 4.2 g of this powder was dispersed in 40 mL of deionized water, followed by the addition of 4.5 mL of aqueous ammonia under vigorous stirring. This resulting homogeneous suspension was placed into a 200 mL Teflon-lined stainless-steel autoclave and heated to 120 °C for 8 h. After the reaction was completed, the autoclave was left to cool down to room temperature overnight. The final mixture was then filtered and centrifuged at 15,000 rpm for 30 min. The clear supernatant, which contained the CQDs, was collected for subsequent use.

2.3 Synthesis of CQDs/ZIF-8

The CQDs/ZIF-8 composite was prepared using an impregnation method [20]. The process began by dissolving 4.5 g of 2-methylimidazole in 100 mL of methanol. In a separate beaker, 2.5 g of zinc nitrate hexahydrate was combined with 4 mL of the previously prepared CQD suspension. This solution was then poured into the 2-methylimidazole-methanol mixture under vigorous stirring, which was maintained for one hour. The combined dispersion was left overnight, after which the solid product was collected via filtration and dried at 60 °C for several hours. Finally, the dried composites were rinsed three times with deionized water to eliminate any residual reactants and then dried once more before being used.

2.4 Characterization of CQDs/ZIF-8

For characterization, a Scanning Electron Microscopy (SEM) (JOEL, JSM-IT200, Japan) was used to analyse the morphology of the composite. The functional groups present in the samples were identified using Fourier Transform Infrared spectroscopy (FTIR) (iS10 Nicolet, Thermo Scientific, USA) over a wavenumber range of 4000 to 500 cm^{-1} using KBr powder to prepare the samples. Additionally, X-ray Diffraction (XRD) was used to observe the crystallographic structure of composite. The optical properties of the materials and the effect of MB removal by the CQDs/ZIF-8 under various conditions were evaluated using UV-Vis Spectroscopy (Agilent Cary 60).

2.5 Adsorption studies of MB

The adsorption tests were performed using a digital orbital shaker set to 200 rpm. The investigation focused on the effects of several parameters: initial MB concentration (5–25 ppm), contact time (30–120 min), adsorbent dosage (10–50 mg), and pH (adjusted using 0.1 M HCl or 0.1 M NaOH) [21]. For each test, 50 mL of MB solution was placed in a centrifuge tube and processed at room temperature. After completing the adsorption phase, the adsorbent was removed from the mixture, and the residual MB concentration was quantified at 664 nm by using UV-Vis spectroscopy. The quantity of dye adsorbed per gram of adsorbent (q_e, mg g^{-1}) and the removal percentage (R, %) were calculated using Eqs. (1) and (2), respectively:

$$\mathrm{q_e} = \frac{\mathrm{C_0} - \mathrm{C_i}}{\mathrm{m}} \times \mathrm{V} \tag{1}$$

Table 1 Linear and non-linear expression of adsorption kinetic models

Types of isotherm models	Non-linear expression	Linear expression	
Langmuir	$q_{cal} = \frac{q_m K_L C_e}{1 + K_L C_e}$	$\frac{C_e}{q_{cal}} = \left(\frac{1}{q_m K_F}\right) + \frac{C_e}{q_m}$	(3)
Freundlich	$q_{cal} = K_F C_e^{1/n}$	$\ln q_{cal} = \ln K_F + \frac{1}{n} \ln C_e$	(4)
Temkin	$q_{cal} = \left(\frac{RT}{B_T}\right) \ln (K_T C_e)$	$q_{cal} = \frac{RT}{B_t} \ln K_t + \frac{RT}{B_t} \ln C_e$	(5)
Dubinin-Radushkevich	$q_{cal} = q_m e^{-\beta\varepsilon}$	$\ln q_{cal} = \ln q_m - \beta\varepsilon^2$	(6)

Table 2 List of linear and non-linear forms of kinetic models

Types of kinetic models	Non-linear expressions	Linear expressions	
Pseudo-first order	$q_t = q_e \left(1 - e^{-k_1 t}\right)$	$\ln \left(\frac{C_i}{C_t}\right) = k_1 t$	(7)
Pseudo-second order	$q_t = \frac{q_e^2 k_2 t}{1 + q_e k_2 t}$	$\frac{t}{q_t} = \frac{1}{k_2 q_e^2} + \frac{t}{q_e}$	(8)
Elovich	$q_t = \left(\frac{1}{\beta}\right) \ln \alpha\beta + \left(\frac{1}{\beta}\right) \ln t$	$q_t = \frac{\ln(\alpha\beta)}{\beta} + \frac{\ln t}{\beta}$	(9)

$$\mathrm{R}\% = \frac{\mathrm{C}_0 - \mathrm{C}_\mathrm{i}}{\mathrm{C}_0} \times 100\% \tag{2}$$

where C_0(mg/L) is the initial concentration of MB dye before adsorption, and *Ci* (mg/L) is the concentration of MB after adsorption has occurred. The variable *m* (g) represents the mass of the adsorbent used, and *V* (L) is the volume of the MB solution.

2.6 Adsorption isotherm studies of MB

The equilibrium relationship between the solid adsorbent and the liquid solution was analyzed using adsorption isotherm models. These experiments were carried out with initial MB concentrations ranging from 5 to 25 ppm, while maintaining 10 mg of CQDs/ZIF-8 dosage, pH 10 for the initial dye concentration, and a contact time of 120 min. The following isotherm models, detailed in Table 1, were applied:

- Langmuir isotherm: This model presupposes monolayer adsorption onto a homogeneous surface.
- Freundlich isotherm: This model describes adsorption on a heterogeneous surface.
- Temkin isotherm: This model accounts for interactions between adsorbate molecules and assumes a linear decrease in the heat of adsorption.
- Dubinin-Radushkevich (D-R) isotherm: This model characterizes physical adsorption within porous structures.

In the models, q_{cal} (m g^{-1}) is the calculated adsorption capacity, q_{max} (mg g^{-1}) is the optimum adsorption capacity for MB, and C_e (mg/L) is the equilibrium concentration of MB. The parameter *n* indicates the favorability of the adsorption process in the Freundlich model, while B_T represents the maximum binding energy. The constants K_L, K_F, K_T, and K_{DR} correspond to the adsorption equilibrium constants for their respective models.

2.7 Adsorption kinetic studies of MB

The kinetics of the adsorption process were investigated over contact times ranging from 20 to 120 min, using a fixed initial MB concentration of 5 ppm, an adsorbent dosage of 10 mg, and a pH of 10. The experimental data were analyzed using the following listed models including linear and non-linear forms of which are provided in Table 2 (Eqs. 7–9). The equations define q_e (mg g^{-1}) as the theoretical MB uptake at equilibrium,

t (min) as the elapsed contact time, C_i and C_t as the initial and time-specific adsorbate concentrations, and q_t (mg g^{-1}) as the amount adsorbed at a given t. The pseudo-first-order and pseudo-second-order kinetics are characterized by the constants k_1 (min^{-1}) and k_2 (g mg^{-1} min^{-1}), respectively. In Elovich framework, α (mg g^{-1} min^{-1}) represents the initial adsorption rate, while β (g mg^{-1}) denoted the desorption coefficient.

2.8 Error analysis

The accuracy of the applied models was assessed using both linear and non-linear regression analyses. The performance of each model was measured with three statistical metrics: the coefficient of determination (R^2), the sum of squared errors (SSE), and the root mean square error (RMSE) [22]. A model is considered to have a better fit when it demonstrates a higher R^2 value concurrently with lower SSE and RMSE values. The formulas for these metrics are provided in Table 3 (Eqs. 10–12).

3 Results and discussions

3.1 Characterization of composites

3.1.1 SEM

The morphology and surface characteristics of the synthesized materials were analyzed using Scanning Electron Microscopy (SEM) at magnifications of ×2000 and ×5000. Figure 1a illustrates the morphology of sago *hampas* granules, which present as spherical to oval particles with highly irregular and non-uniform sizes. The CQDs display a markedly rough and uneven surface, a texture that can be ascribed to the vigorous mechanical and chemical pre-treatment processes. These steps may have disrupted the cell wall structure, giving rise to a coarse and irregular surface morphology, as illustrated in Fig. 1b.

Furthermore, SEM micrograph of ZIF-8 (Fig. 1c) shows a distinct rhombic dodecahedron shape with sharp edges and relatively small, evenly distributed particles. In the CQDs/ZIF-8 composite (Fig. 1d), both materials retained their individual structural morphology. However, the CQDs were observed to be smaller and uniformly anchored onto the surface of ZIF-8, signifying successful hybridization between the two components.

After adsorption of the MB dye removal (Fig. 1e), CQDs/ZIF-8 adsorbate surface became noticeably rougher compared to the pristine composite. This increased roughness is attributed to the accumulation of MB molecules at the active sites, confirming the efficient adsorption of dye molecules onto the CQDs/ZIF-8 framework.

3.1.2 FTIR analysis

The spectrum of CQDs have revealed a series of distinct peaks, each attributable to different functional groups, as shown in Fig. 2 [23]. The broad around 3475 cm^{-1} was assigned to O-H stretching vibrations, indicating the presence of hydroxyl groups

Table 3 List of error functions and expressions

Error functions	Error function expressions	
Coefficient of determination (R^2)	$\frac{\sum_{i=1}^{n}(q_{cal}-q_{\exp})^2}{\sum_{i=1}^{n}(q_{cal}-q_{\exp})^2}$	(10)
Sum of the squares of the error (SSE)	$\sum_{i=1}^{n}(q_{\exp}-q_{cal})^2$	(11)
Root means square error (RMSE)	$\sqrt{\frac{\sum_{i=1}^{n}(q_{\exp}-q_{cal})^2}{N}}$	(12)

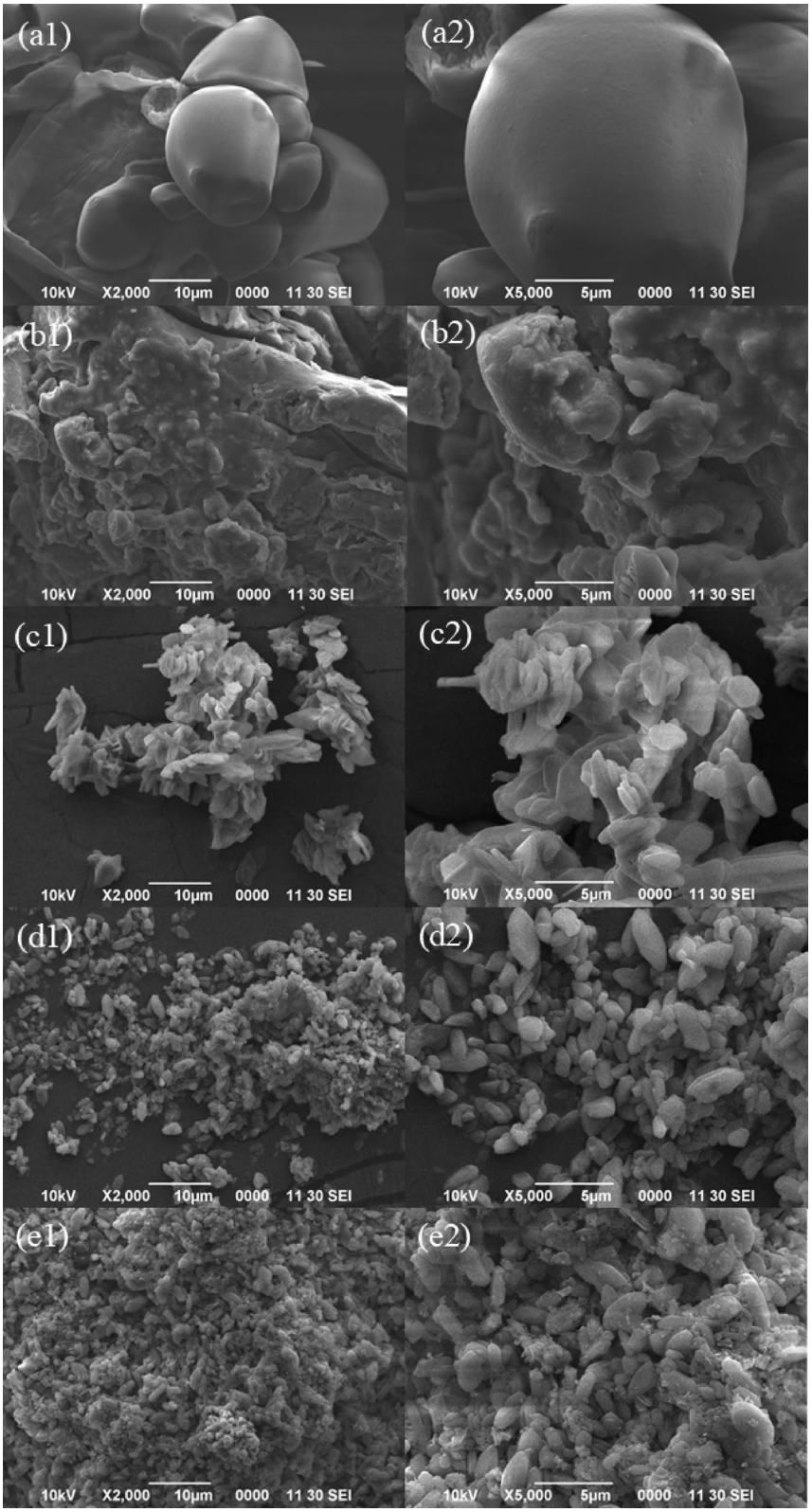

Fig. 1 SEM images of **a** sago *hampas*, **b** CQDs **c** ZIF-8, **d** CQDs/ZIF-8 before adsorption and **e** CQDs/ZIF-8 after adsorption at magnification of 2000x and 5000x

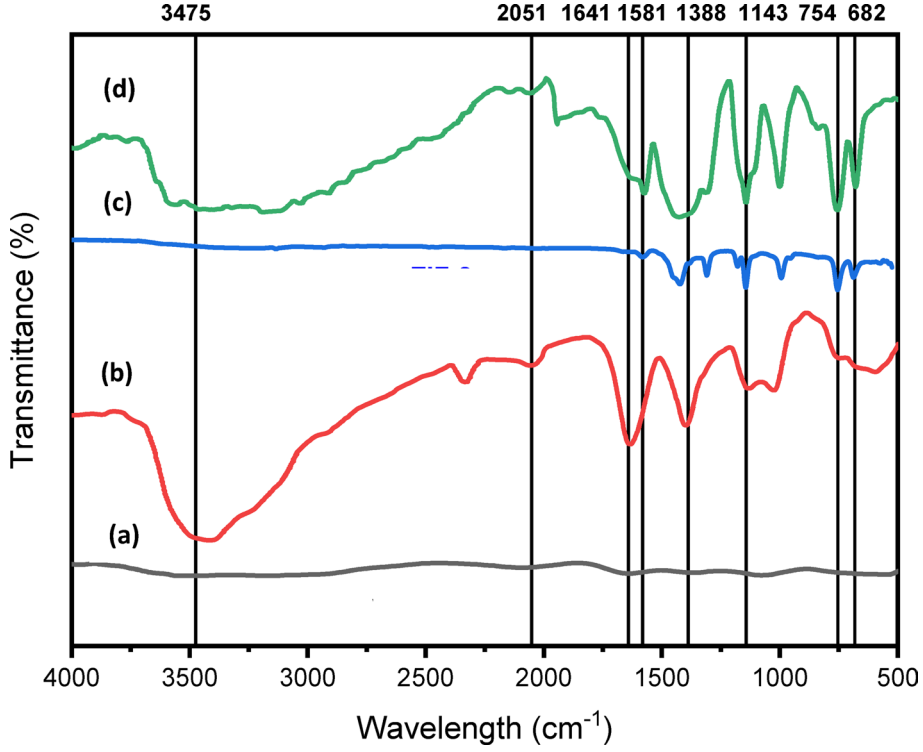

Fig. 2 FTIR spectra of **a** sago hampas, **b** CQDs, **c** ZIF-8 and **d** CQDs/ZIF-8

capable of forming hydrogen bonds or engaging in electrostatic interactions with cationic dye molecules such as MB. Furthermore, the peaks at 1388 cm^{-1}, 2054 cm^{-1} and 754 cm^{-1} corresponded to C = C and C-H stretching vibrations, representing aromatic and aliphatic carbon structures that can facilitate π–π interactions with the aromatic rings of MB [24].

However, for ZIF-8 the distinctive peak at 682 cm^{-1} was attributed to Zn-N stretching vibrations, confirming the coordination between zinc ions and imidazole linkers. Additional bands appearing at 754 cm^{-1}, 1143 cm^{-1} and 1581 cm^{-1} were assigned to C-H, C-N and C = N stretching vibrations, respectively [25]. These functional groups are essential for adsorption, as Zn-N sites can attract negatively charged Mb groups via electrostatic interactions.

The CQDs/ZIF-8 composite's FTIR spectrum displayed characteristic peaks corresponding to both CQDs and ZIF-8, confirming their successful integration. The presence of hydroxyl (-OH) and carbonyl (C = O) groups from CQDs, along with Zn-N coordination from ZIF-8, indicates multiple adsorption mechanisms, including hydrogen bonding, electrostatic attraction, and π–π stacking between MB molecules and the composite surface. These synergistic effects collectively enhance the overall adsorption capacity of the CQDs/ZIF-8 material.

3.1.3 XRD analysis

The XRD patterns of CQDs, ZIF-8, and CQDs/ZIF-8 are shown in Fig. 3. The CQDs exhibited a broad diffraction peak around $2\theta \approx 23°$, suggesting their amorphous nature and the formation of extremely small crystallite domains [26]. The broad peak

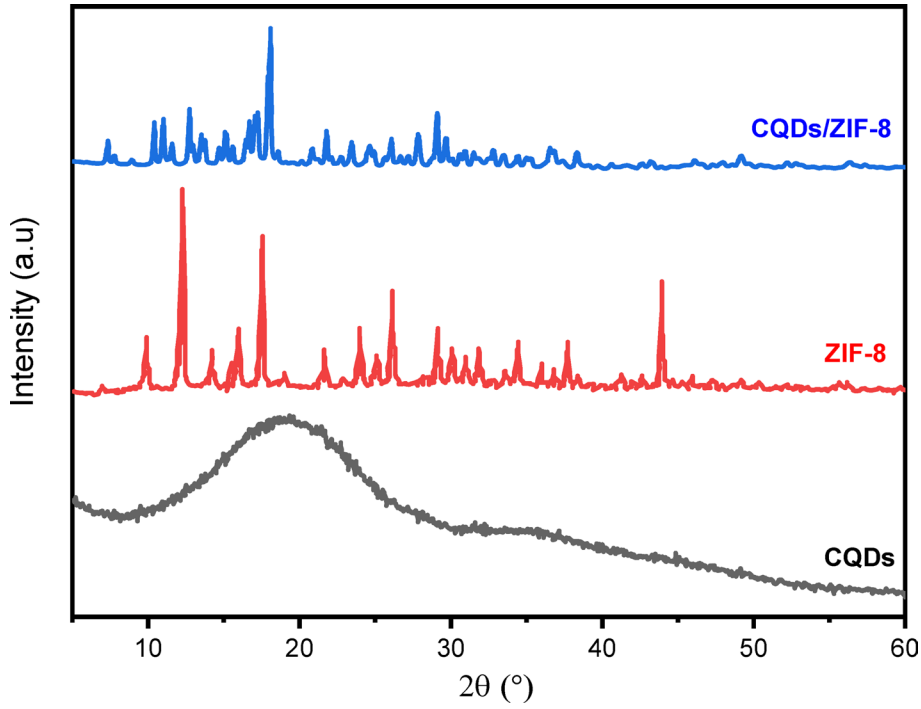

Fig. 3 The XRD pattern of CQDs, ZIF-8 and CQDs/ZIF-8

is consistent with the Scherrer equation (Eq. 13), which states that diffraction peaks broaden as crystallite size decreases.

For ZIF-8, several sharp diffraction peaks were detected in the 5°-45° range, with prominent reflections at 10.10°, 12.26°, 14.22°, 16.12°, and 18.08°, corresponding to the (011), (002), (112), (022), and (013) planes, respectively. These peaks confirm the formation of a highly crystalline ZIF-8 structure [27]. The XRD pattern of CQDs/ZIF-8 showed similar diffraction peaks to that of pure ZIF-8, verifying that the crystalline framework of ZIF-8 remained intact after CQD incorporation. The absence of a distinct CQD peak can be attributed to their low crystallinity and uniform dispersion within the ZIF-8 matrix. The sharp, well-defined peaks in both ZIF-8 and CQDs/ZIF-8 indicate that the composite maintains high crystallinity [11, 23].

The crystallite size of CQDs/ZIF-8 was calculated using the Scherrer equation:

$$D = \frac{K\lambda}{\beta \cos\theta} \tag{13}$$

when $K = 0.9$ is the shape factor, $\lambda = 1.5406$ Å is the X-ray wavelength (Cu Kα), β *is* the full width at half maximum (FWHM) in radians, and θ is the Bragg angle. Based on the most intense diffraction peak at $2\theta = 17.98°$ with FWHM = 0.130°, the calculated crystallite size was approximately 61 nm. This nanoscale crystallite dimension supports the presence of well-structured ZIF-8 domains and indicates that the incorporation of CQDs did not disrupt the crystallinity of ZIF-8. The small crystallite size contributes to an enlarged surface area and increased availability of active sites, which are advantageous for dye adsorption applications.

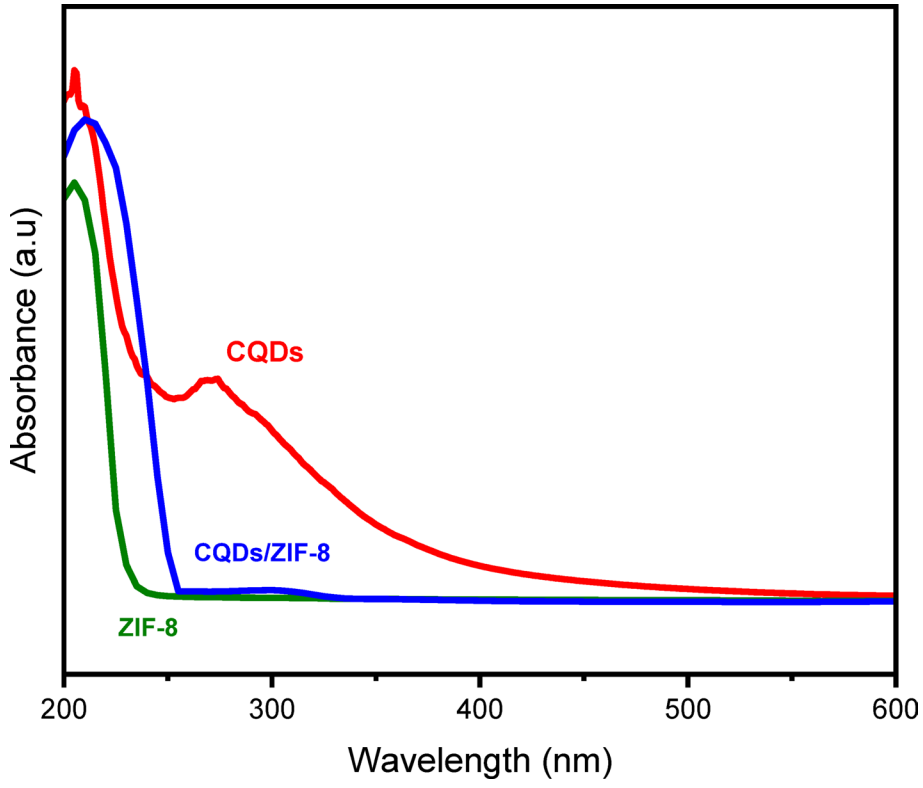

Fig. 4 Comparison of UV-Vis spectra for CQDs, ZIF-8 and CQDs/ZIF-8

3.1.4 UV-Vis analysis

The optical characteristics of the synthesized materials were investigated using a UV-Vis spectrophotometer, as illustrated in Fig. 4. The CQDs displayed a distinct absorption peak near 275 nm, corresponding to the $n \rightarrow \pi^*$ and $\pi \rightarrow \pi^*$ electronic transitions associated with the C = O and C = C bonds, respectively [28, 29]. This characteristic absorption indicates the successful formation of CQDs containing conjugated carbon domains and oxygen-bearing functional groups. In contrast, ZIF-8 exhibited no significant absorption in the UV region, consistent with its weak light-absorption capacity due to its wide band gap. The CQDs/ZIF-8 composite showed a faint absorption peak around 275 nm, similar to that of pure CQDs, confirming that CQDs were successfully incorporated onto the ZIF-8 surface without altering their intrinsic optical characteristics [30].

Furthermore, both CQDs and CQDs/ZIF-8 displayed strong fluorescence emissions under UV illumination, as shown in Fig. 5, respectively. The fluorescence behavior of CQDs arises from their quantum confinement effect and surface passivation, while the preserved luminescent property in the composite suggests efficient electronic interaction between the CQDs and the ZIF-8 framework. The observed optical activity not only confirms successful CQD incorporation but also implies potential photo-activated adsorption behavior. The photo-excited electrons and holes generated within the CQDs under UV or visible light may enhance dye degradation or adsorption efficiency through synergistic photochemical effects.

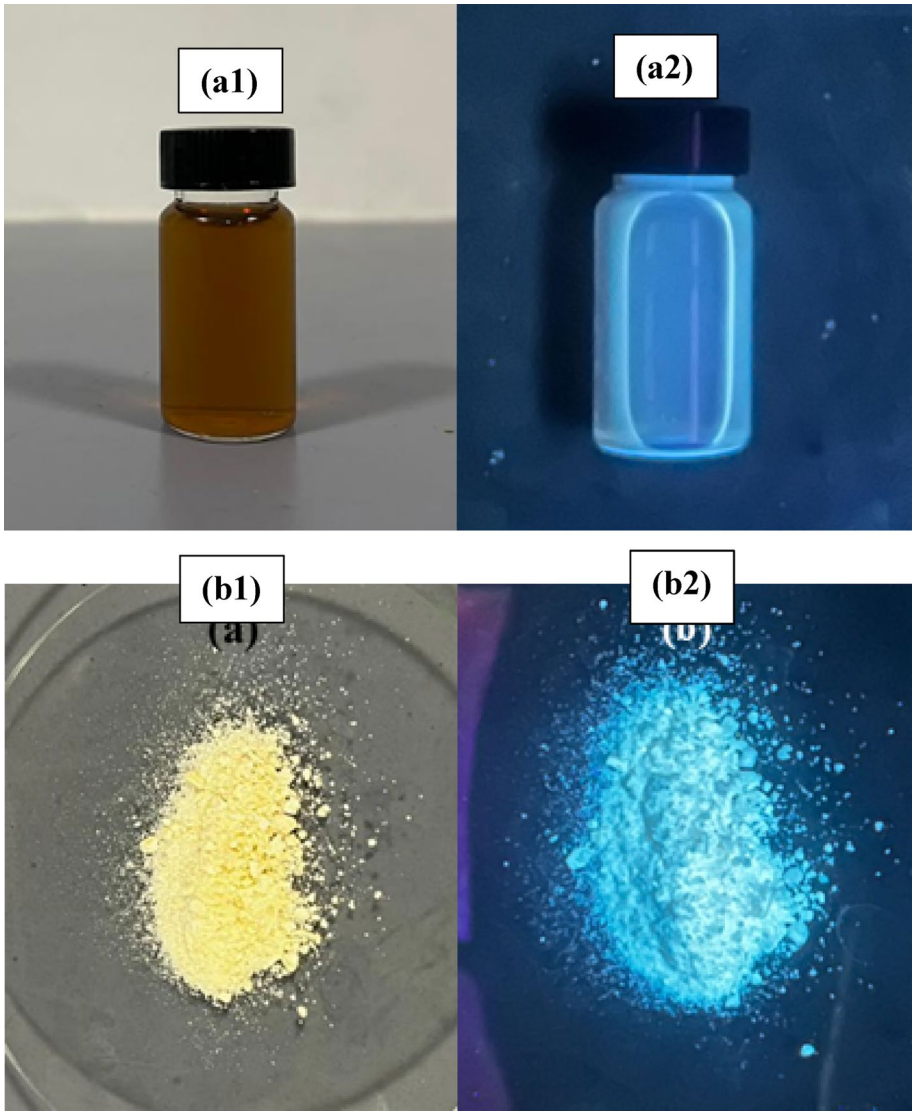

Fig. 5 The **a** CQDs solution and **b** CQDs/ZIF-8 composite under (1) visible light and (2) UV light with the wavelength of 365 nm

3.2 Effects of parameters on adsorption of MB dye

The adsorption capacity and removal efficiency of MB were analyzed under different experimental parameters, including pH, initial dye concentration, contact time, and adsorbent dosage.

3.2.1 Effect of initial MB pH on solution properties

Figure 6 illustrates the influence of pH (2–10) on MB removal using 10 mg of adsorbent, a 120 min contact time, and an initial MB concentration of 5 ppm.

An increase in pH from 2 to 10 significantly improved MB removal efficiency, rising from 19.12% to 88.60%, while the adsorption capacity increased from 6.57 mg g^{-1} to 30.42 mg g^{-1}. At lower pH, an excess of H^+ ions competes with the positively charged MB molecules for adsorption sites, leading to reduce adsorption performance [31]. Moreover, at higher pH levels, the oxygen-containing functional groups on CQDs/ZIF-8 undergo deprotonation, generating a negatively charged surface that enhances

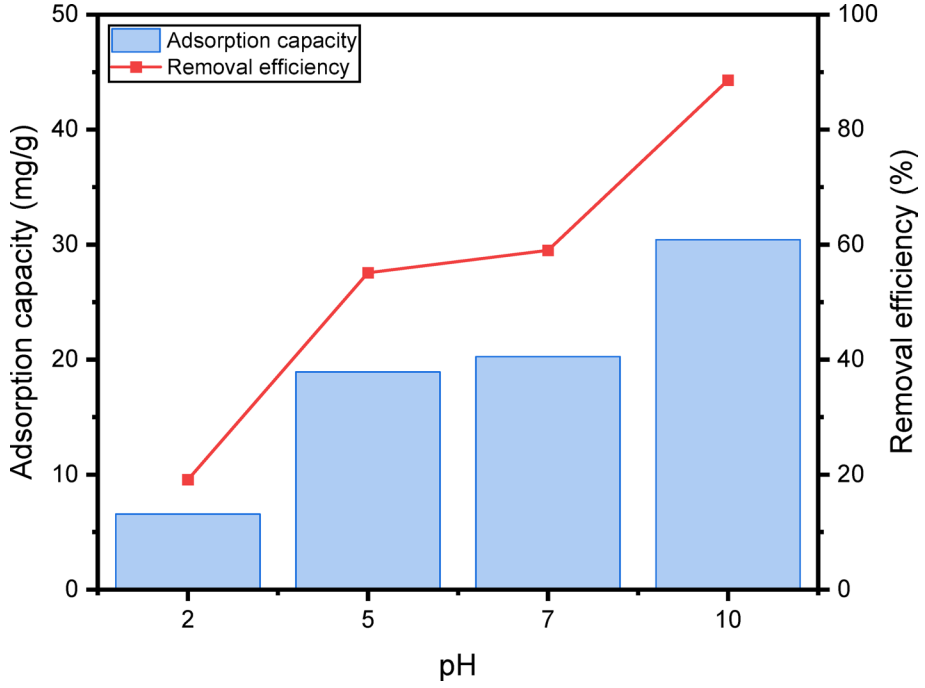

Fig. 6 Initial pH impact on MB removal efficiency and adsorption capacity of CQDs/ZIF-8 (10 mg adsorbent, 50 mL, 5 ppm, 80 min)

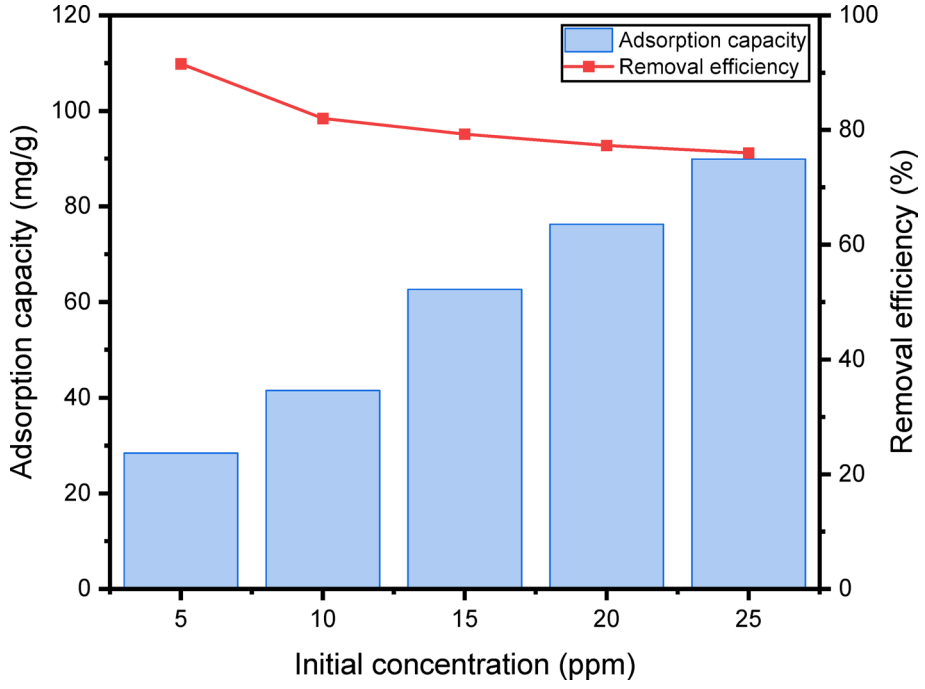

Fig. 7 Initial concentration impact on MB removal efficiency and adsorption capacity of CQDs/ZIF-8 (10 mg adsorbent, 50 mL, pH 10, 120 min)

electrostatic attraction toward cationic MB molecules. This surface charge transformation accounts for the improved adsorption capacity and removal efficiency under alkaline conditions [14].

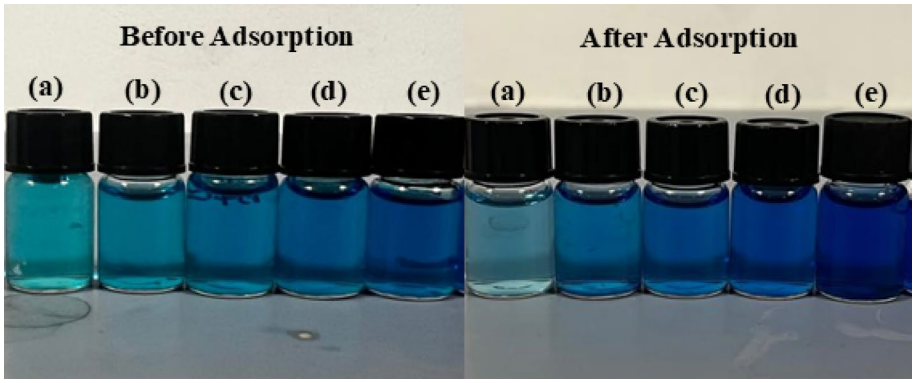

Fig. 8 Colour changes of **a** 5 ppm, **b** 10 ppm, **c** 15 ppm, **d** 20 ppm and **e** 25 ppm MB solutions before and after adsorption test

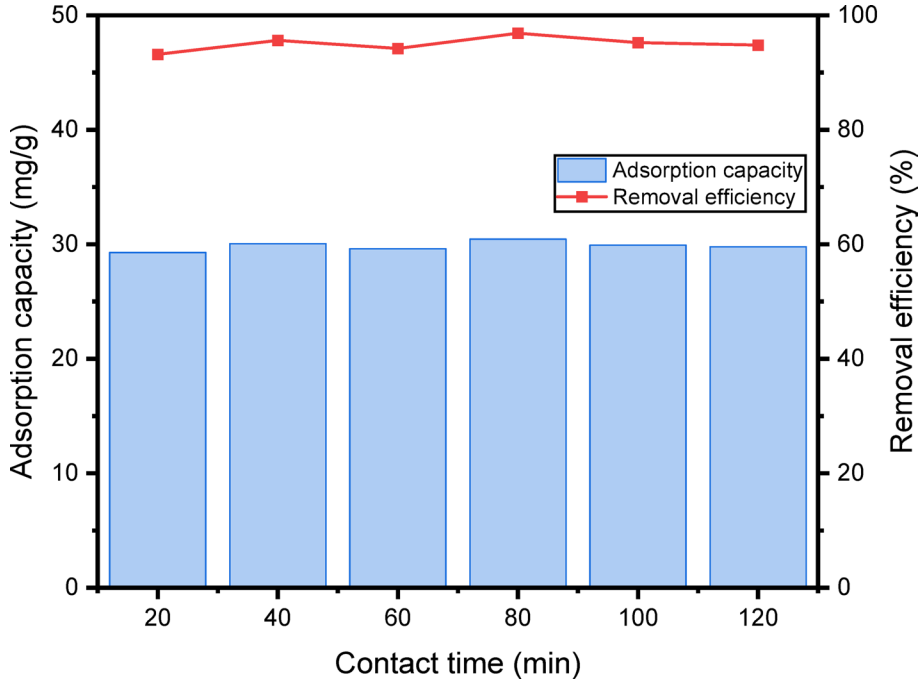

Fig. 9 Contact time impact on MB removal efficiency and adsorption capacity of CQDs/ZIF-8 (10 mg adsorbent, 50 mL, pH 10, 5 ppm)

3.2.2 Effect of initial MB concentration on solution properties

Figure 7 depicts the impact of the initial MB concentration on adsorption behavior under fixed conditions (10 mg adsorbent, pH 10, 120 min contact time). As the MB concentration increased from 5 ppm to 25 ppm, the removal efficiency decreased from 91.6% to 76.0% due to saturation of available adsorption sites at higher dye loading. Conversely, the adsorption capacity increased with concentration, reaching a maximum of approximately 89.9 mg g^{-1} at 25 ppm, as more dye molecules occupied active sites in the adsorbent surface. This inverse relationship, higher capacity but lower percentage removal, correlates with adsorption-site saturation [32]. Figure 8 shows the colour changes of MB before and after adsorption test.

3.2.3 Effect of contact time of MB removal and solution properties

Figure 9 shows how varying contact time (20–120 min) affects MB adsorption when 10 mg of CQDs/ZIF-8 was used at pH 10 and an initial dye concentration of 5 ppm. During the first 20 min, dye uptake increased sharply, achieving an adsorption capacity of 29.30 mg g^{-1} and a removal efficiency of 93.20%. This rapid initial phase is attributed to the abundance of vacant active sites on the adsorbent surface. As contact time increases, adsorption slowed, reaching equilibrium around 80 min with capacity of 30.44 mg g^{-1} and removal efficiency of 96.88%. The plateau at this stage indicates near-saturation of available binding sites, where further adsorption becomes limited. The overall kinetic process thus shows an initial diffusion-driven phase followed by site saturation typical of chemisorption behavior [33, 34].

3.2.4 Effect of adsorbent dosage on MB removal

Figure 10 illustrate how adsorbent dosages (10–50 mg) affecting the MB removal efficiency and adsorption capacity at pH 10 and an initial MB concentration of 5 ppm. As the adsorbent mass increased, removal efficiency improved, reaching a maximum of 82.64% at 30 mg. This enhancement is associated with the increased surface area and the availability of more active sites and pores for MB adsorption [35–37]. However, as the dosage rose from 10 mg to 50 mg, the adsorption capacity declined markedly from 23.78 mg g^{-1} to 5.09 mg g^{-1} demonstrating the inverse relationship between dosage and adsorption capacity [38]. In addition, the removal efficiency modestly dropped from 82.64% to 81.69% when dosage increase beyond 30 mg, indicating that 30 mg represents the optimal amount for maximum MB removal.

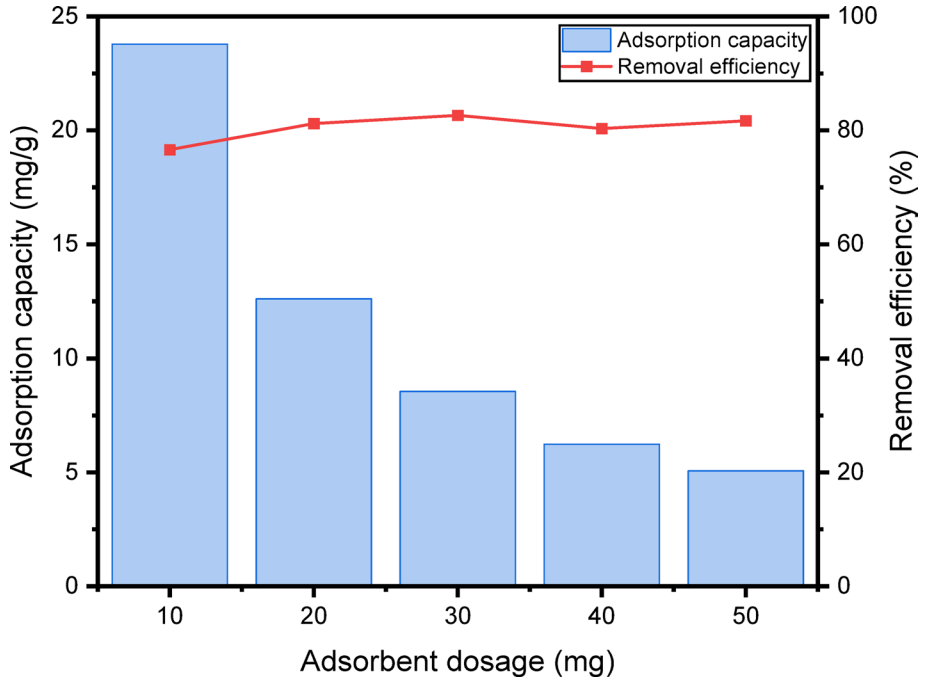

Fig. 10 Adsorbent dosage impact on MB removal efficiency and adsorption capacity of CQDs/ZIF-8 (80 min, 50 mL, 5 ppm, pH 10)

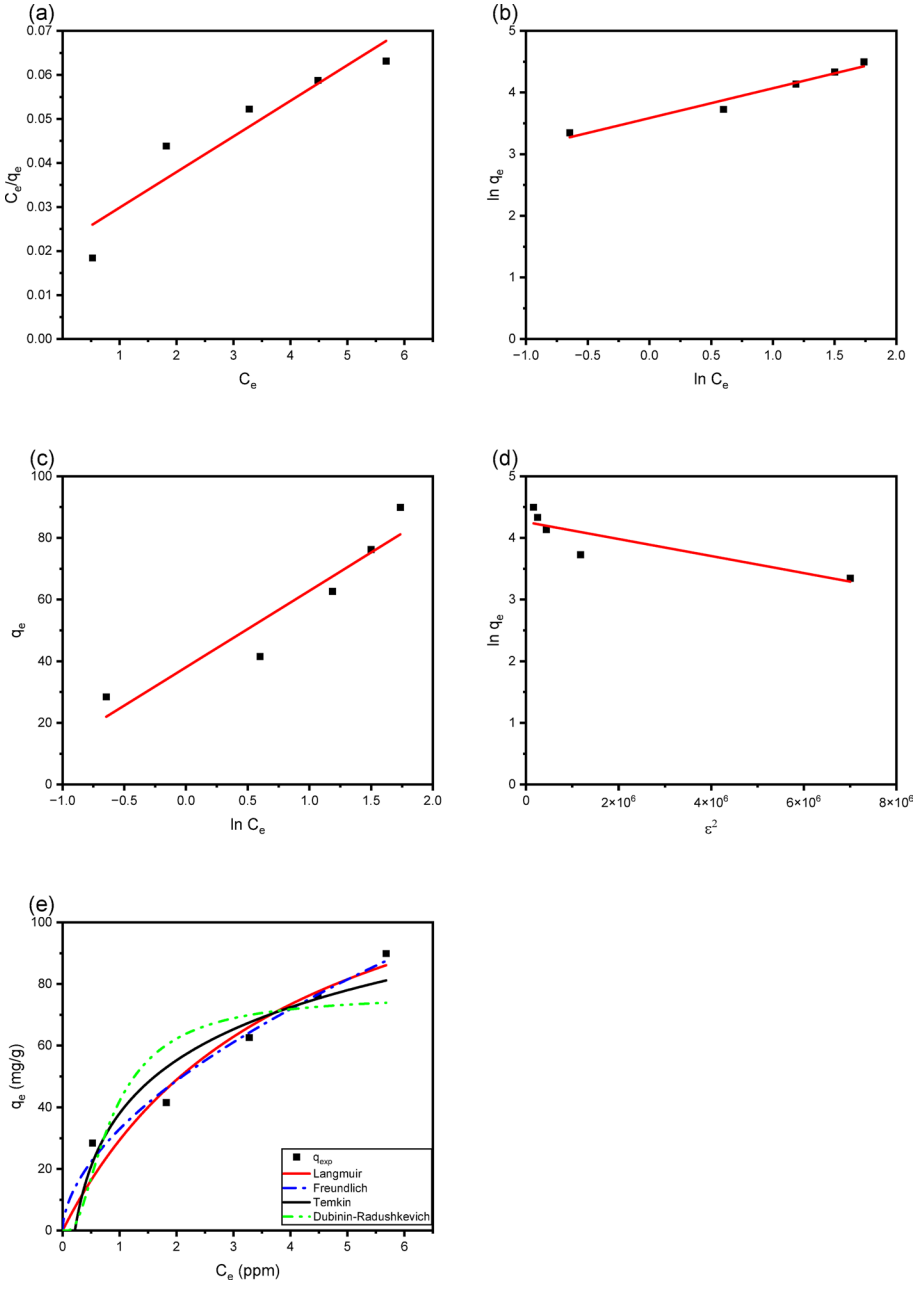

Fig. 11 Linear plots of **a** Langmuir, **b** Freundlich, **c** Temkin, **d** Dubinin-Radushkevich and **e** non-linear isotherms on the adsorption capacity of MB dye

3.3 Adsorption isotherm analysis

Linear and non-linear adsorption were evaluated (Fig. 11a–e), and the corresponding error-function metrics are compiled in Table 4. These error analyses were used to determine which isotherm model provided the best fit based on minimum error values. Among the linearized models (Fig. 11a–d), the Freundlich isotherm exhibited the highest correlation coefficient (R^2 = 0.9484), while the Langmuir, Temkin, and Dubinin-Radushkevich (D-R) models showed lower R^2 values of 0.8419, 0.8552, and 0.6601, respectively. The Freundlich model also produced the smallest sum of squared errors

Table 4 Data obtained from linear and non-linear isotherm models

Model		Parameter	Value
Langmuir	Linear	q_m	46.00
		K_L	2.68
		R^2	0.8419
		SSE	207.46
		RMSE	6.44
	Non-linear	q_m	146.70
		K_L	0.25
		R^2	0.9595
		SSE	177.41
		RMSE	5.96
Freundlich	Linear	n	2.07
		K_F	36.08
		R^2	0.9484
		SSE	94.64
		RMSE	4.35
	Non-linear	n	1.63
		K_F	30.68
		R^2	0.9863
		SSE	60.06
		RMSE	3.47
Temkin	Linear	B_T	24.83
		K_T	4.63
		R^2	0.8552
		SSE	272.02
		RMSE	7.38
	Non-linear	B_T	38.83
		K_T	1.70
		R^2	0.8642
		SSE	272.02
		RMSE	7.38
Dubinin-Radushkevich	Linear	q_m	70.81
		K_{DR}	1.38×10^{-7}
		R^2	0.6601
		SSE	855.98
		RMSE	13.08
	Non-linear	q_m	76.38
		K_{DR}	1.24
		R^2	0.6165
		SSE	768.41
		RMSE	12.40

(SSE) and root mean square error (RMSE) values, further validating its superior fitting performance.

When comparing linear and non-linear isotherm analyses, the non-linear models exhibited consistently lower error values, indicating a better fit overall. Among them, the Freundlich model again proved most suitable, achieving an R^2 of 0.9863, compared to the Langmuir (0.9595), Temkin (0.9642), and D-R (0.6165) models.

The dominance of the Freundlich isotherm indicates that MB adsorption onto CQDs/ZIF-8 occurs on a heterogeneous surface with multilayer adsorption behavior. This agrees with the surface characteristics of the composite, in which CQDs introduce multiple active functional groups (-OH, -COOH, -NH_2) exhibiting varied affinities toward

MB molecules. These sites enable diverse adsorption mechanisms, including electrostatic attraction between negatively charged groups and cationic MB, π–π interactions between aromatic structures, and surface complexation involving Zn-N sites within ZIF-8.

3.3.1 Adsorption kinetics analysis

The MB adsorption kinetics were fitted with pseudo-first-order, pseudo-second-order, and Elovich models (Fig. 12a–d) and the kinetic parameters derived from each model are summarized in Table 5.

Form the linear kinetic plots (Fig. 12a–c), the pseudo-second-order model provided the best fitted with R^2 of 0.9995, whereas the pseudo-first-order and Elovich models yielded much lower R^2 values of 0.4506 and 0.1138, respectively. The pseudo-second-order model also exhibited the smallest SSE and RMSE values, indicating an excellent fit for describing the adsorption behavior.

The non-linear kinetic analysis (Fig. 12d) revealed similar results where the pseudo-second-order model also achieved the most best-fitter R^2 of 0.9993, surpassing the pseudo-first-order (0.9963) and Elovich (0.9955) models. The calculated maximum adsorption capacity (30.18 mg g^{-1}) was closely matched the experimental value (30.44 mg g^{-1}), confirming strong agreement between theoretical predictions and experimental data. According to Table 5, non-linear models consistently showed lower error values than their liner plots, emphasizing that the non-linear pseudo-second-order model most accurately represents the adsorption kinetics of MB onto CQDs/ZIF-8.

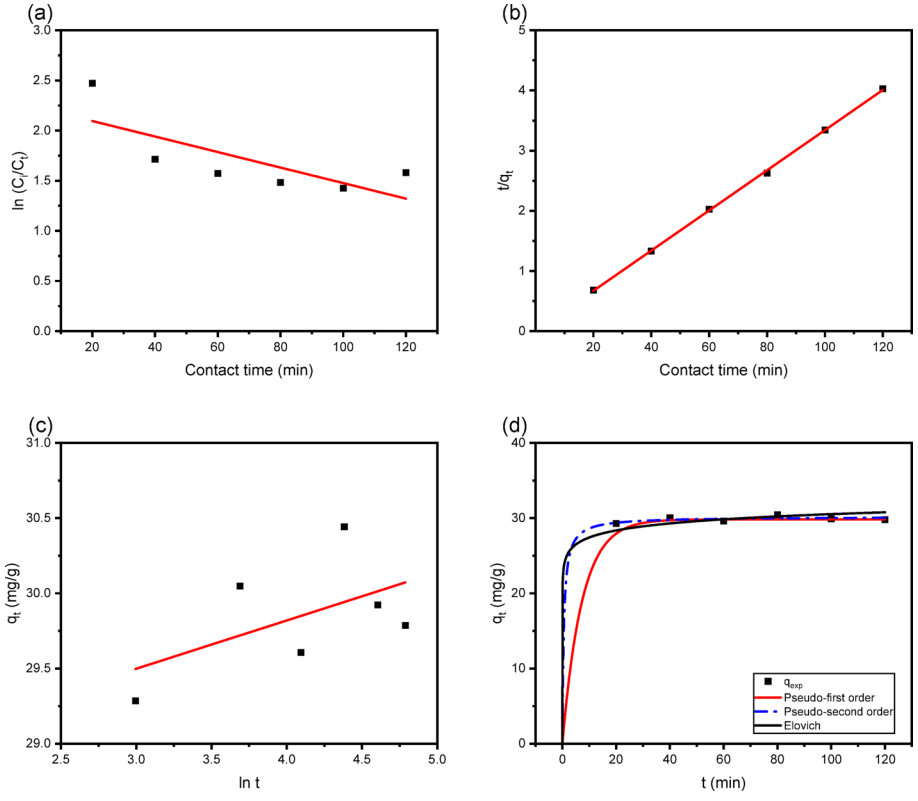

Fig. 12 The adsorption kinetic linear models **a** Pseudo-First-Order, **b** Pseudo-Second-Order, **c** Elovich and **d** non-linear model on the adsorption capacity of MB

Table 5 Data obtained from linear and non-linear kinetic models

Model		Parameter	Value
Pseudo-first order	Linear	q_e	9.49
		K_1	-6.45×10^{-5}
		R^2	0.4506
		SSE	438.90
		RMSE	8.55
	Non-linear	q_e	29.83
		K_1	0.14
		R^2	0.9963
		SSE	2.37
		RMSE	0.63
Pseudo-second order	Linear	q_e	29.98
		K_2	0.30
		R^2	0.9995
		SSE	0.21
		RMSE	0.18
	Non-linear	q_e	30.18
		K_2	0.06
		R^2	0.9993
		SSE	0.47
		RMSE	0.28
Elovich	Linear	β	28.54
		α	0.32
		R^2	0.1138
		SSE	883.30
		RMSE	12.13
	Non-linear	β	9.34
		α	0.74
		R^2	0.9955
		SSE	2.86
		RMSE	0.69

Table 6 The comparison of previous study for methylene blue dye removal

Adsorbent	Adsorption capacity (mg g^{-1})	References
Ag_2S/GO/CQDs	348	[39]
CQD/CNT	299.4	[40]
rPET/MWNT/CQD	12.45	[41]
MK/CQD	154.07	[42]
Leaf shaped ZIF-8	205	[43]
ZIF-8	25	[44]
ZIF-8	242	[5]
Fe_3O_4/ZIF-8	20	[45]
CQDs/ZIF-8	89.92	This study

The excellent fit of the pseudo-second-order model indicates that chemisorption predominates, where adsorption depends on the number of active sites and the process entails electrons being shared or transferred between the dye molecules and the functional groups on CQDs/ZIF-8. Specifically, nitrogen- and oxygen-containing groups (-NH, -OH, -COOH) in CQDs and Zn-N coordination sites in ZIF-8 participate in strong chemical interactions such as surface complexation, hydrogen bonding, and electrostatic attraction with MB molecules. These interactions enhance the stability of the adsorbed layer, confirming that the process follows a chemisorption mechanism.

3.4 A comparative studies of MB adsorption efficiencies across different adsorbents

Table 6 summarizes the MB dye's adsorption capacities on various adsorbents studied by previous researchers alongside the present work. The CQDs/ZIF-8 composite exhibited an adsorption capacity of 89.92 mg g^{-1}, which was significantly higher than Fe_3O_4/ZIF-8 (20 mg g^{-1}) and rPET/MWNT/CQD (12.45 mg g^{-1}) and comparable to CQD/CNT (299 mg g^{-1}). These differences stem from the varying surface areas, pore structure, and the abundance of active functional groups among adsorbents.

The relatively high adsorption capacity of CQDs/ZIF-8 can be attributed to the synergistic interaction between CQDs and the ZIF-8 framework. Incorporation of CQDs introduces oxygen- and nitrogen-containing functional groups (-OH, -COOH, $-NH_2$), which enhance surface polarity and create additional binding sites for MB through hydrogen bonding and electrostatic interactions. Meanwhile, ZIF-8 contributes a large surface area and microporous structure that facilitates π–π interactions between the imidazolate rings and the aromatic MB molecules.

Although certain nanocomposites, such as Ag_2S/GO/CQDs, display even higher adsorption capacities, these materials often require costly or non-sustainable precursors. By contrast, the present CQDs/ZIF-8 composite was synthesized from sago waste, offering an environmentally friendly and cost-effective alternative with excellent adsorption efficiency. Thus, this material demonstrates strong potential for sustainable dye-removal applications, combining high performance with ecological and economic benefits.

4 Conclusions

Successful synthesis of CQDs and CQDs/ZIF-8 composites was achieved by employing hydrothermal and impregnation techniques, as verified by SEM, FTIR, XRD, and UV-Vis analyses. Optimal conditions for MB removal were established at an initial dye concentration of 5 ppm, pH 10, 80 min contact time, and 30 mg adsorbent dosage. Regression analysis indicated that non-linear models provided a better fit than linear ones, with the Freundlich isotherm best describing equilibrium adsorption and the pseudo-second-order model accurately representing the kinetics, both showing high R^2 and low SSE/RMSE values. The remarkable adsorption performance of CQDs/ZIF-8 stems from its heterogeneous surface and abundance of active functional groups, which enable multiple dye-adsorbent interactions. Overall, this study demonstrates that CQDs/ZIF-8 is a promising, sustainable, and cost-effective material for efficient dye removal in wastewater treatment applications.

Acknowledgements
The authors are thankful to Ministry of Higher Education Malaysia through Fundamental Research Grant Scheme FRGS (grant number: FRGS/1/2024/STG04/UNIMAS/02/1) for funding this study.

Author contributions
DNAC designed the study, developed the team, and contributed majorly to the original draft's write-up. NAK and NAAS conducting the research and investigation process, specifically performing the experiments and completing the write-up, MAMA participated in the write up. MAM Amin supervised the study and helped in proofreading. All authors reviewed the manuscript.

Funding
Open Access funding provided by Universiti Malaysia Sarawak. This research received financial support from the Ministry of Higher Education Malaysia via the Fundamental Research Grant Scheme (FRGS), grant number FRGS/1/2024/STG04/UNIMAS/02/1.

Data availability
The datasets used in this study are available from the corresponding author upon reasonable request.

Declarations

Ethics approval and consent to participate
Not applicable.

Consent for publication
All authors give their consent to publish.

Competing interests
The authors declare no competing interests.

Received: 14 October 2025 / Accepted: 17 December 2025
Published online: 25 December 2025

References

1. Khan R, Shukla S, Kumar M, Barceló D, Zuorro A, Bhargava PC. Progress and Obstacles in employing carbon quantum dots for sustainable wastewater treatment. Environ Res. 2024;234:119671. https://doi.org/10.1016/j.envres.2024.119671.
2. Anush SM, et al. Graphene oxide functionalized chitosan-magnetite nanocomposite for removal of Cu(II) and Cr(VI) from waste water. Int J Biol Macromol. 2020;164:1234–45. https://doi.org/10.1016/j.ijbiomac.2020.09.059.
3. Mahmoudi MM, Nadali A, Arezoomand HRS, Mahvi AH. Adsorption of cationic dye textile wastewater using clinoptilolite: isotherm and kinetic study. J Text Inst. 2019;110(1):56–64. https://doi.org/10.1080/00405000.2018.1465329.
4. Mu Y, Ma H. NaOH-modified mesoporous biochar derived from tea residue for methylene blue and Orange II removal. Chem Eng Res Des. 2021;167:432–44. https://doi.org/10.1016/j.cherd.2021.01.008
5. Mirzaei K, Mohammadi A, Jafarpour E, Shojaei A, Moghaddam AL. Improved adsorption performance of ZIF-8 towards methylene blue dye by hybridization with nanodiamond. J Water Process Eng. 2022;50:103254. https://doi.org/10.1016/j.jwpe.2022.103254.
6. Alinejad A, et al. High adsorption of methylene blue from aqueous solutions using leaf-shaped ZIF-8. Int J Environ Anal Chem. 2021;101(14):2354–67. https://doi.org/10.1080/03067319.2019.1702170
7. Elaouni A, El Ouardi M, Zbair M, BaQais A, Saadi M, Ait Ahsaine H. ZIF-8 metal organic framework materials as a superb platform for the removal and photocatalytic degradation of organic pollutants: a review. R Soc Chem. 2022;12:4500–21. https://doi.org/10.1039/d2ra05717d
8. Mo Z, Tai DZ, Zhang H, Shahab A. A comprehensive review on the adsorption of heavy metals by zeolite imidazole framework (ZIF-8) based nanocomposite in water. Chem Eng J. 2022;443:136320. https://doi.org/10.1016/j.cej.2022.136320.
9. Dai H, et al. Recent advances on ZIF-8 composites for adsorption and photocatalytic wastewater pollutant removal: fabrication, applications and perspective. Coord Chem Rev. 2021;441:213985. https://doi.org/10.1016/j.ccr.2021.213985.
10. Duan C, Ma T, Wang J, Zhou Y. Removal of heavy metals from aqueous solution using carbon-based adsorbents: a review. J Water Process. 2020;37:101339. https://doi.org/10.1016/j.jwpe.2020.101339.
11. Liu Q, Gao X, Liu Z, Gai L, Yue Y, Ma H Sensitive and selective electrochemical detection of Lead(II) based on waste-biomass-derived carbon quantum Dots@Zeolitic imidazolate framework-8. Materials. 2023;16(9):3378. https://doi.org/10.3390/ma16093378.
12. Tan XW, Romainor ANB, Chin SF, Ng SM. Carbon dots production via pyrolysis of Sago waste as potential probe for metal ions sensing. J Anal Appl Pyrol. 2014;105:157–65. https://doi.org/10.1016/j.jaap.2013.11.001.
13. Atchudan R, Jebakumar Immanuel Edison TN, Shanmugam M, Perumal S, Somanathan T, Lee YR. Sustainable synthesis of carbon quantum dots from banana Peel waste using hydrothermal process for in vivo bioimaging. Phys E Low Dimens Syst Nanostruct. 2021;126:114417. https://doi.org/10.1016/j.physe.2020.114417.
14. He M, Zhang J, Wang H, Kong Y, Xiao Y, Xu W. Material and optical properties of fluorescent carbon quantum dots fabricated from lemon juice via hydrothermal reaction. Nanoscale Res Lett. 2018;13(1):175. https://doi.org/10.1186/s11671-018-2581-7.
15. Arumugam N, Kim J. Synthesis of carbon quantum dots from broccoli and their ability to detect silver ions. Mater Letter. 2018;219:129–33. https://doi.org/10.1016/j.matlet.2018.02.043.
16. Hui KC, Ang WL, Sambudi NS. Nitrogen and bismuth-doped rice husk-derived carbon quantum dots for dye degradation and heavy metal removal. J Photochem Photobiol A. 2021;418:113411. https://doi.org/10.1016/j.jphotochem.2021.113411.
17. Manikandan V, Lee NY. Green synthesis of carbon quantum Dots and their environmental applications. Environ Res. 2022;212:113283. https://doi.org/10.1016/j.envres.2022.113283.
18. Siruru H, Syafii W, Wistara INJ, Pari G, Budiman I. Properties of sago waste charcoal using hydrothermal and pyrolysis carbonization. Biomass Convers Biorefinery. 2022;12(12):567–75. https://doi.org/10.1007/s13399-020-00983-9
19. Rajamanikandan S, Biruntha M, Ramalingam G. Blue emissive carbon quantum dots (CQDs) from bio-waste peels and its antioxidant activity. J Cluster Sci. 2021;33(3):1045–53. https://doi.org/10.1007/s10876-021-02029-0
20. Si Y, Li X, Yang G, Mie X, Ge L. Fabrication of a novel core–shell CQDs@ZIF-8 composite with enhanced photocatalytic activity. J Mater Sci. 2020;55(27):13049–61. https://doi.org/10.1007/s10853-020-04909-8
21. Gemici BT, Ozel HU, Ozel HB. Removal of methylene blue onto forest wastes: adsorption isotherms, kinetics and thermodynamic analysis. Environ Technol Innov. 2021;22:101501. https://doi.org/10.1016/j.eti.2021.101501.
22. Benmessaoud A, Nibou D, Mekatel EH, Amokrane S. A comparative study of the linear and non-linear methods for determination of the optimum equilibrium isotherm for adsorption of Pb^{2+} ions onto Algerian treated clay. Iran J Chem Chem Eng. 2020;39(4):153–71. https://doi.org/10.30492/ijcce.2020.39755.
23. Nurmalasari N, Lestari SJ, Syamsuddin M, Sukarti S, Alam MN. Thermal stability analysis of cellulose from Sago fiber waste (Metroxylon sago). EduChemia J Kimia Pendidik. 2022;7(2):182–92. https://doi.org/10.30870/educhemia.v7i2.13491.
24. Almufarij RS, Mohamed ME. Green synthesis of a carbon quantum dots-based superhydrophobic membrane for efficient oil/water separation. Materials. 2023;16(15):5456. https://doi.org/10.3390/ma16155456

25. Zhang Y, Jia Y, Li M, Hou L. Influence of the 2-methylimidazole/zinc nitrate hexahydrate molar ratio on the synthesis of zeolitic imidazolate framework-8 crystals at room temperature. Sci Rep. 2018;8(1):9597. https://doi.org/10.1038/s41598-018-28015-7.
26. Safardoust-Hojaghan H, Salavati-Niasari M, Amiri O, Rashki S, Ashrafi M. Green synthesis, characterization and antimicrobial activity of carbon quantum dots-decorated ZnO nanoparticles. Ceram Int. 2021;47(4):5187–97. https://doi.org/10.1016/j.ceramint.2020.10.097.
27. Ostad MI, Shahrak MN, Galli F. The influence of different synthetic solvents on photocatalytic activity of ZIF-8 for methanol production from CO_2. Microporous Mesoporous Mater. 2021;326:111363. https://doi.org/10.1016/j.micromeso.2021.111363.
28. Singh H, Bamrah A, Khatri M, Bhardwaj N. One-pot hydrothermal synthesis and characterization of carbon quantum dots (CQDs). Mater Today Proc. 2020;28(3):1891–4. https://doi.org/10.1016/j.matpr.2020.05.297
29. Wang N, Wang Y, Guo T, Yang T, Chen M, Wang J Green Preparation of carbon Dots with Papaya as carbon source for effective fluorescent sensing of iron (III) and *Escherichia coli*. Biosens Bioelectron. 2016;85:68–75. https://doi.org/10.1016/j.bios.2016.04.089.
30. Si Y, Li X, Yang G, Mie X, Ge L. Fabrication of a novel core–shell CQDs@ZIF-8 composite with enhanced photocatalytic activity. J Mater Sci. 2020;55(27):13049–61. https://doi.org/10.1007/s10853-020-04909-8
31. Li Y, Gao C, Jiao J, Cui J, Li Z, Song Q. Selective adsorption of metal-organic framework toward methylene blue: behavior and mechanism. ACS Omega. 2021;6(49):33961–8. https://doi.org/10.1021/acsomega.1c05299
32. Kuang Y, Zhang X, Zhou S. Adsorption of methylene blue in water onto activated carbon by surfactant modification. Water. 2020;12(2):587. https://doi.org/10.3390/w12020587.
33. Gemici BT, Ozel HU, Ozel HB. Removal of methylene blue onto forest wastes: adsorption isotherms, kinetics and thermodynamic analysis. Environ Technol Innov. 2021;22:101501. https://doi.org/10.1016/j.eti.2021.101501.
34. Deniz F, Kepekci RA. Bioremoval of malachite green from water sample by forestry waste mixture as potential biosorbent. Microchem J. 2017;132:172–8. https://doi.org/10.1016/j.microc.2017.01.015.
35. Alamin NU, et al. Activated carbon-alginate beads impregnated with surfactant as sustainable adsorbent for efficient removal of methylene blue. Int J Biol Macromol. 2021;176:233–43. https://doi.org/10.1016/j.ijbiomac.2021.02.017.
36. Fito J, Abrham S, Angassa K. Adsorption of methylene blue from textile industrial wastewater onto activated carbon of parthenium hysterophorus. Int J Environ Res. 2020;14(5):501–11. https://doi.org/10.1007/s41742-020-00273-2.
37. Paluri P, Ahmad KA, Durbha KS. Importance of estimation of optimum isotherm model parameters for adsorption of methylene blue onto biomass derived activated carbons: comparison between linear and non-linear methods. Biomass Convers Biorefinery. 2022;12(9):4031–48. https://doi.org/10.1007/s13399-020-00867-y.
38. Do TH, et al. Study on methylene blue adsorption of activated carbon made from *Moringa oleifera* leaf. Materials Today Proc. 2021;38(5):3405–13. https://doi.org/10.1016/j.matpr.2020.10.834
39. Zhang D, et al. Synthesis of a novel CQDs-GO-Ag_2S composite and study on the adsorption of methylene blue. ChemistrySelect. 2020;5(8):2501–7. https://doi.org/10.1002/slct.202000102
40. Chen Q, et al. One-step synthesis of carbon quantum dot-carbon nanotube composites on waste eggshell-derived catalysts for enhanced adsorption of methylene blue. J Environ Chem Eng. 2021;9(5):106222. https://doi.org/10.1016/j.jece.2021.106222.
41. Mallakpour S, Behranvand V. Synthesis of mesoporous recycled poly(ethylene terephthalate)/MWNT/carbon quantum dot nanocomposite from sustainable materials using ultrasonic waves: application for methylene blue removal. J Clean Prod. 2018;190:525–37. https://doi.org/10.1016/j.jclepro.2018.04.120.
42. Sambudi NS, et al. Modification of kaolin with carbon quantum dots as composite for methylene blue removal: literature review and experiment. Indones J Sci Technol. 2022;7(2):311–36. https://doi.org/10.17509/ijost.v7i2
43. Alinejad A, et al. High adsorption of methylene blue from aqueous solutions using leaf-shaped ZIF-8. Int J Environ Anal Chem. 2021;101(14):2354–67. https://doi.org/10.1080/03067319.2019.1702170
44. Santoso E, et al. Facile synthesis of ZIF-8 nanoparticles using polar acetic acid solvent for enhanced adsorption of methylene blue. Microporous Mesoporous Mater. 2021;310:110620. https://doi.org/10.1016/j.micromeso.2020.110620.
45. Zheng J, et al. Surfactant-free synthesis of a Fe_3O_4@ ZIF-8 core–shell heterostructure for adsorption of methylene blue. CrystEngComm. 2014;16(19):3960–4. https://doi.org/10.1039/c3ce42648c.